Chemical Engineering Science 117 (2014) 407–415

Contents lists available at ScienceDirect

Chemical Engineering Science

journal homepage: www.elsevier.com/locate/ces

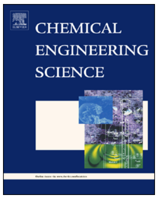

Transient breakthroughs of CO_2/CH_4 and C_3H_6/C_3H_8 mixtures in fixed beds packed with Ni-MOF-74

De-Li Chen [a], Hao Shang [a], Weidong Zhu [a,*], Rajamani Krishna [b,*]

[a] Key Laboratory of the Ministry of Education for Advanced Catalysis Materials, Institute of Physical Chemistry, Zhejiang Normal University, 321004 Jinhua, PR China
[b] Van't Hoff Institute for Molecular Science, University of Amsterdam, Science Park 904, 1098 XH Amsterdam, The Netherlands

HIGHLIGHTS

- Highly selective separation of C_3H_6 over C_3H_8 and CO_2 over CH_4 on Ni-MOF-74.
- Simulation methodology for transient breakthroughs in fixed-bed adsorbers.
- Inclusion of intra-crystalline diffusion improves the quality of the simulations.
- Good agreement between breakthrough experiments and simulations.
- Ni-MOF-74 is a promising candidate for C_3H_6/C_3H_8 and CO_2/CH_4 separations.

GRAPHICAL ABSTRACT

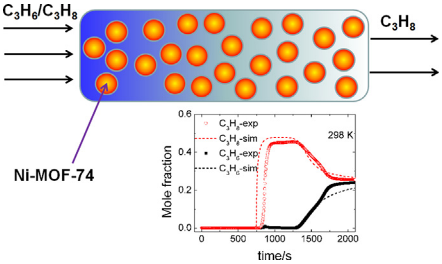

ARTICLE INFO

Article history:
Received 30 April 2014
Received in revised form
29 June 2014
Accepted 1 July 2014
Available online 11 July 2014

Keywords:
Metal-organic frameworks
Fixed-bed adsorber
Light olefin/paraffin separation
CO_2 adsorption
Intra-crystalline diffusion

ABSTRACT

The metal-organic framework Ni-MOF-74 was synthesized and then characterized by XRD, SEM, and N_2 adsorption techniques. The unary isotherms of CO_2, CH_4, C_3H_6, and C_3H_8 on Ni-MOF-74 were measured by means of a volumetric method. The Langmuir–Freundlich model appropriately describes the adsorption equilibrium data. The selective separations of two mixtures CO_2/CH_4 and C_3H_6/C_3H_8 on Ni-MOF-74 were experimentally investigated by a breakthrough-column technique. Simulations of transient breakthroughs for the two mixtures agree well with the experimental data. In addition, with the inclusion of intra-crystalline diffusion into the simulations, the quality of the simulated breakthrough curves are improved and agree better with the experimental data. The results indicate that Ni-MOF-74 might be a candidate for the removal of C_3H_6 from C_3H_6/C_3H_8 mixtures and for the efficient separation of CO_2 from CH_4.

1. Introduction

During the last two decades, there has been considerable research effort on synthesis of ordered crystalline microporous materials such as metal-organic frameworks (MOFs), covalent-organic frameworks (COFs), and zeolitic imidazolate frameworks (ZIFs) (Banerjee et al., 2008; Ferey, 2008; Furukawa et al., 2013; Yaghi et al., 2003); these materials have potential applications in a variety of separations (Furukawa et al., 2013; He et al., 2012; Haldoupis et al., 2010; Krishna, 2014; Krishna and van Baten, 2010, 2011a; Li et al., 2012; Liu et al., 2012; Sumida et al., 2012; Watanabe et al., 2009). MOFs are a class of crystalline organic–inorganic hybrid compounds formed by coordination of metal ions (e.g., Zn, Cu, Cr, Al, Zr, Mg, Ni, Fe) or clusters with organic linkers (bivalent or trivalent aromatic carboxylic acids or azoles) to form

---

[*] Corresponding authors.
E-mail addresses: weidongzhu@zjnu.cn, wzhudelft@yahoo.com (W. Zhu), r.krishna@contact.uva.nl (R. Krishna).

http://dx.doi.org/10.1016/j.ces.2014.07.008
0009-2509/© 2014 Elsevier Ltd. All rights reserved.

robust porous periodic frameworks. Particularly potent candidates for separations are MOFs with coordinatively unsaturated metal clusters that may be created by evacuation of frameworks that have metal-bound solvent molecules. This strategy has been employed to expose M^{2+} cation sites in some of the most widely studied frameworks, such as M_2(dobdc) [M = Mg, Mn, Co, Ni, Zn, Fe; $dobdc^{4-}$ = 2,5-dioxido-1,4-benzenedicarboxylate; these MOFs are also referred to as M-MOF-74 and CPO-27-M, as shown in Fig. 1 (a)] (Bao et al., 2011a, 2011b; Britt et al., 2008; Herm et al., 2011, 2012; Wu et al., 2014).

For CO_2 capture from natural gas, we can rely on selective CO_2 binding with the coordinatively unsaturated metal sites of M-MOF-74, where the presence of small cylindrical pores is believed to be also a key structural feature (Caskey et al., 2008). Wu et al. (2010) have established that the O atoms of CO_2 bind with the Mg atoms of Mg-MOF-74 [see Fig. 1(b)]. Such binding results in selective separations that can compete economically with amine absorption (Alivisatos and Buchanan, 2010; Bao et al., 2011b; Dietzel et al., 2008; Duan et al., 2014; Herm et al., 2012; Krishna and van Baten, 2012a; Mason et al., 2011; McDonald et al., 2011; Padurean et al., 2012; Wu et al., 2012; Xiang et al., 2012; Yang et al., 2014; Yu et al., 2013). The stronger the binding, the higher is the selectivity for separations. It was reported that the binding of H_2S with metal atoms of MOFs is much stronger than that with CO_2, and this is reflected in a high heat of adsorption (Chavan et al., 2013). In this case, the binding is between the S atoms with Ni sites of Ni-MOF-74 [Fig. 1(c)]. Kizzie et al. (2011) have shown that Mg-MOF-74 is particularly sensitive to the presence of water impurities in the feed stream, whereas Co-MOF-74 and Ni-MOF-74 are less sensitive in this regard. Liu et al. (2012, 2010) have reported that Ni-MOF-74 retains a substantial CO_2 capacity with moderate H_2O loading, and by comparison with other adsorbents such as the benchmark zeolites 5A and NaX and the MOF CuBTC, Ni-MOF-74 shows a higher CO_2 adsorption capacity and the smaller water effect together with an easier regeneration process, suggesting that Ni-MOF-74 may be a promising candidate for removal of CO_2 from flue gases.

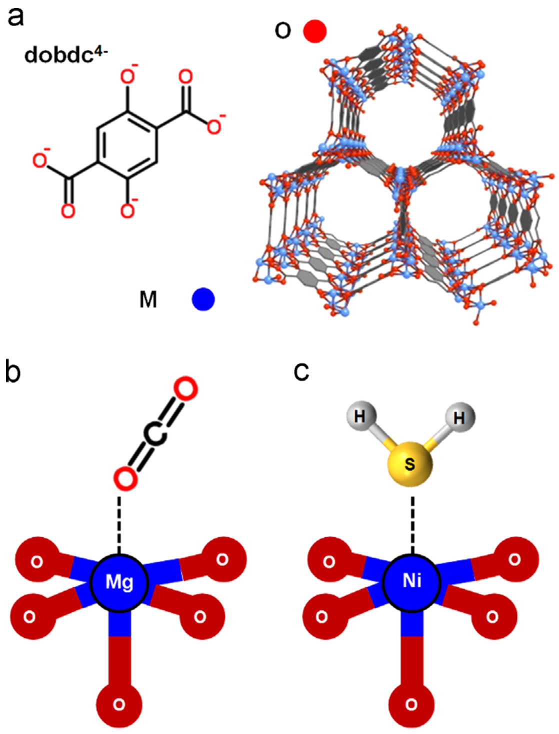

Fig. 1. (a) Scheme of M-MOF-74 crystal structure, where the red and blue balls represent oxygen and metal atoms, respectively, and energetically favorable binding pattern for (b) CO_2 and (c) H_2S on M-MOF-74. (For interpretation of the references to color in this figure legend, the reader is referred to the web version of this article.)

As a consequence of the similar sizes and volatilities of the molecules, separations of olefin/paraffin mixtures, such as C_2H_4/C_2H_6 and C_3H_6/C_3H_8, must currently be performed at low temperatures and high pressures and are among the most energy-intensive separations carried out on a large scale in the chemical industry (Eldridge, 1993). Because these gas mixtures are produced by cracking long-chain hydrocarbons at elevated temperatures, a substantial energy penalty arises from cooling the gases to the low temperatures required for distillation. Thus, tremendous energy savings could be realized if porous solid adsorbents enabling the efficient separation of olefins and paraffins at higher temperatures (than currently used in distillation) and atmospheric pressure were achieved (Geier et al., 2013). In general, there are two mechanisms for the separations of light olefins and paraffins by porous materials (Eldridge, 1993). The first one is based on kinetic or even molecular-sieve effects to discriminate between paraffins and olefins. For example, C_3H_6 can be selectively adsorbed on the all-silica zeolites DD3R (Zhu et al., 1999, 2000) and ITQ-32 (Palomino et al., 2007) while C_3H_8 cannot, leading to an extremely high selectivity for C_3H_6 over C_3H_8. However, the applications of these zeolitic adsorbents are largely limited to their difficulty in synthesis. The second mechanism is based on porous adsorbents featuring selective chemical interactions with the carbon-carbon double bond in olefins (Eldridge, 1993). Commercial zeolite 13X (Da Silva and Rodrigues, 1999) and CuCl/NaX (van Miltenburg et al., 2008) show a high selectivity for C_3H_6 over C_3H_8. However, the regeneration of hydrophilic zeolite-based adsorbents is difficult in applied vacuum swing adsorption (VAS) processes at temperatures as low as 298 K (van Miltenburg et al., 2008). Increasing the operating temperature can improve this, but high temperatures can lead to C_3H_6 oligomerization and possibly cracking owing to catalytic action of these materials, eventually blocking the adsorbents. In addition, these hydrophilic zeolites are sensitive to moisture. Separations by adsorption via π-complexation are susceptible to deactivation by feed contaminants (Eldridge, 1993).

Recently, some interesting results have been obtained on the separations of olefins and paraffins using MOFs (Nijem et al., 2012). For example, fine-tuning of the ligands in zeolitic imidazolate framework ZIF-8 leads to a very large ratio of their diffusion coefficients up to 125 for C_3H_6/C_3H_8 (Li et al., 2009), where the efficient adsorptive separation should be controlled by the critically sized pore openings of ZIF-8. The windows of ZIF-8 have a nominal size of 0.34 nm; the window regions offer large energy barriers for inter-cage hopping of molecules that have kinetic diameters of comparable magnitudes (Bux et al., 2011; Chmelik et al., 2012; Krishna and van Baten, 2011b). Subtle differences in the bond lengths and bond angles of C_3H_6 and C_3H_8 are the main contributory factors to the significantly higher diffusivity of the unsaturated alkene (Krishna and van Baten, 2012b).

In addition, using the gate-opening mechanism of microporous materials the efficient separation of light hydrocarbon mixtures was also achieved (Gucuyener et al., 2010; Nijem et al., 2012). Alternatives are the MOFs with coordinatively unsaturated metal sites since these unsaturated metal sites in the framework bind stronger to olefins over paraffins (Bao et al., 2011a; Bloch et al., 2012; Böhme et al., 2013; Kim and Jung, 2014; Kim et al., 2013; Wu et al., 2014). Bloch et al. (2012) have demonstrated that Fe-MOF-74 has some excellent performance on separating C_2H_4/C_2H_6 and C_3H_6/C_3H_8 mixtures, since the unsaturated metal Fe sites can selectively adsorb the olefins over the paraffins. The high C_2H_4/C_2H_6 and C_3H_6/C_3H_8 adsorption selectivity with Fe-MOF-74 is due to the side-on π-coordination of the unsaturated alkenes with the

Fe^{2+} (Bloch et al., 2012), whereas the paraffins are adsorbed to the metal site with much weaker interaction. Additionally, by comparison with other adsorbents such as zeolites ITQ-12 and NaX and MOFs CuBTC and Fe-MIL-100, Fe-MOF-74 shows the best performance on the separation of C_3H_6/C_3H_8 mixtures (Bloch et al., 2012). Very recently, Geier et al. (2013) reported the unary isotherms of C_2H_4, C_2H_6, C_3H_6, and C_3H_8 on M-MOF-74 (M=Mg, Mn, Fe, Co, Ni, Zn) and the adsorption selectivities of C_2H_4/C_2H_6 and C_3H_6/C_3H_8 mixtures predicted by the ideal adsorbed solution theory (IAST), and their results show that Mn-MOF-74 and Mg-MOF-74 have the highest gravimetric capacities for C_3H_6. For a fixed-bed adsorber, it is also important to consider the volumetric capacity of an adsorbent, as this will determine the size of bed necessary to capture a given amount of gas. In contrast to the gravimetric capacity, the volumetric capacity is the highest on Ni-MOF-74 for C_3H_6.

The main objective of this study is to demonstrate the potential of Ni-MOF-74 for the separations of C_3H_6/C_3H_8 and CO_2/CH_4 mixtures. We first synthesize Ni-MOF-74, then press the synthesized crystalline particles into the pellets, which are more suitable for scalable industrial application, and finally characterize the prepared samples using different techniques. The single-component isotherms of CO_2, CH_4, C_3H_6, and C_3H_8 on the Ni-MOF-74 pellets are measured and then described by a proper isotherm model. Transient breakthroughs are experimentally determined for the two mixtures CO_2/CH_4 and C_3H_6/C_3H_8 in a fixed bed packed with the Ni-MOF-74 pellets; the experimental transient breakthroughs are compared with simulations using the methodology described in detail in the Supplementary material accompanying this publication. Comparisons of simulated and experimental breakthroughs serve to verify the modeling procedure adopted. Finally, the feasibility of Ni-MOF-74 as applied to CO_2/CH_4 and C_3H_6/C_3H_8 separations is discussed.

2. Materials and methods

2.1. Synthesis and characterization of Ni-MOF-74

Ni-MOF-74 was synthesized, activated, and evacuated according to the procedure reported in the literature (Dietzel et al., 2006). Two solutions, 0.373 g of nickel acetate tetrahydrate in 10 ml of deionized water and 0.149 g of 2,5-dihydroxyterephthalic acid in 10 ml of tetrahydrofuran (THF), were mixed under stirring in a Telflon-lined autoclave for 30 min and the synthesis was carried out without agitation in an oven at 383 K for 3 d. The product was filtered, and the solid was washed with ethanol. The washed solid was then dried at 373 K for 12 h in a vacuum desiccator prior to further analysis or use.

The powdered X-ray diffraction (XRD) patterns were performed on a Philips PW3040/60 diffractometer using Cu$K\alpha$ radiation (λ=0.1541 nm) in a scanning range (2θ) of 2–50°. The morphology and crystal size of the synthesized sample were examined with scanning electron microscopy (SEM). The SEM image was obtained using a Hitachi S-4800 instrument operating at 5.0 kV. The synthesized sample was first pressed at 2 MPa and then crushed into particles with sizes from 0.420 to 0.595 mm in diameter to prepare the pellet sample. The textural properties of the synthesized and pellet samples were evaluated by N_2 adsorption at 77 K using a Micromeritics ASAP 2020 instrument. The samples were outgassed under vacuum at 423 K for 10 h, prior to the adsorption measurements. The grain density of the pellet sample was measured by He pycnometry (Micromeritics AccuPyc II 1340).

2.2. Adsorption isotherms

The single-component adsorption isotherms of CO_2 and CH_4 on the pellet sample were measured by a Particulate Systems HPVA-200 instrument. The sample cell was loaded with ca. 500 mg of the adsorbent. After the adsorbent was outgassed under vacuum at 423 K for 10 h in order to remove any adsorbed impurities, prior to the adsorption measurements, the adsorption runs were carried out at pressures up to 1.2 MPa and three different temperatures (298, 323, and 348 K). The single-component adsorption isotherms of C_3H_6 and C_3H_8 on the pellet sample were measured by the Micromeritics ASAP 2020 instrument, in which the experimental procedure and conditions were the same as those for the CO_2 and CH_4 isotherm measurements with the Particulate Systems HPVA-200, except for the measured pressures up to 120 kPa.

2.3. Transient breakthrough experiments

The flow-sheet diagram of the breakthrough setup is shown in Fig. 2, and the setup consists of three sections: a gas mixing and flow control section, a breakthrough column, and an analysis section. The mixing section contains a total of four mass flow controllers (MFC1-4). The two adsorbing gases are introduced into the mixing section via two mass flow controllers (MFC3 and MFC4) with an operation range of 0–20 ml(STP) min^{-1} (STP: 273 K and 1 atm). The two adsorbing gases can be mixed with He from MFC2 [0–200 ml (STP) min^{-1}]. The desorption gas flow is controlled with MFC1 [0–200 ml(STP) min^{-1}].

The breakthrough column was installed inside the ceramic oven, which was located inside the convection oven. The external

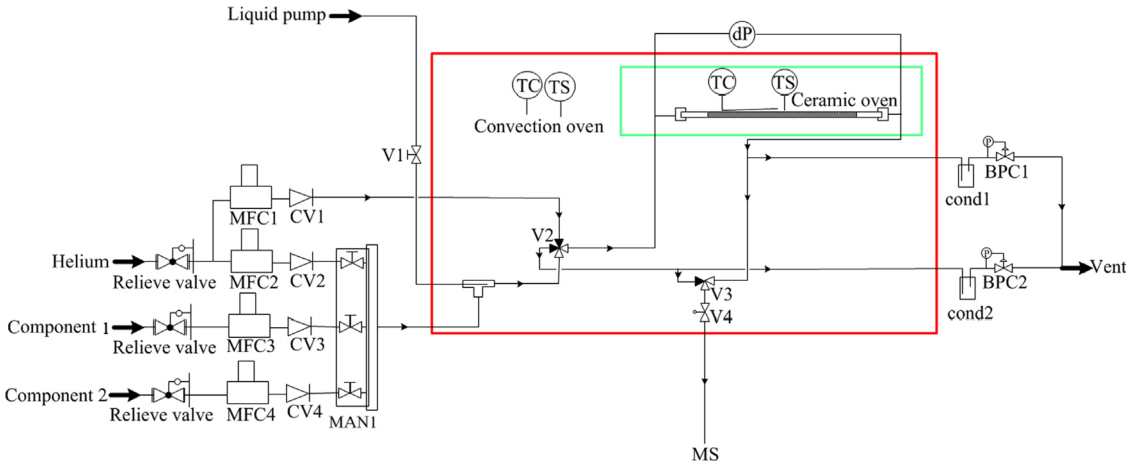

Fig. 2. Flow-sheet diagram of the breakthrough setup.

diameter of the column was 6.35 mm with a length of 10 cm and the inner diameter was 4.65 mm. The pressure drop across the column was monitored by the differential pressure (dp) sensor. The pressure in the outlet of the column was regulated with the back pressure controller (BPC1). The gas flow sent to the analysis section could be adjusted with the needle valve (V4). Selection valve V2 allowed either the feed or purge gas pass the column, and selection valve V3 allowed either the feed or the flow from the outlet of the column to be sent to the analysis section. The mass spectrometer (Pfeiffer Vacuum OmniStar GSD 320) in the analysis section was used to monitor the component concentrations continuously.

The Ni-MOF-74 pellet sample, 576.1 mg, was filled into the column and then heated in flowing He with a rate of 20 ml(STP) min^{-1} at 423 K for 8 h prior to the breakthrough measurements. The breakthrough curves were then measured by switching the He flow to a flow containing CO_2 and CH_4 (or C_3H_6 and C_3H_8) in He (used as a balance) with a CO_2:CH_4:He (or C_3H_6:C_3H_8:He) mole composition of 1:1:2 at a total flow rate of 8 ml(STP) min^{-1}. The breakthrough experiments were performed at three different temperatures (298, 323, and 348 K) and the exit pressure of the breakthrough column was set at 200 kPa, while the pressure drops of the column, which were dependent on the operating temperature and the set exit pressure of the column, were less than 20 kPa under the experimental conditions. After each breakthrough experiment, the column was flushed with flowing He at 20 ml (STP) min^{-1} for 6 h at the measurement temperature.

The used gases had the following purities: CO_2 (99.999%), CH_4 (99.99%), C_3H_6 (99.9%), C_3H_8 (99.9%), and He (99.999%).

3. Results and discussion

3.1. Textural and physical properties of Ni-MOF-74

The XRD pattern of the synthesized sample is identical to that reported in the literature (Dietzel et al., 2006), see Fig. 3, confirming the successful synthesis of Ni-MOF-74. Fig. 4 shows the morphology of the synthesized Ni-MOF-74 by the SEM image, indicating that the sample consists of crystallite agglomerates and the average particle size is less than 4 μm in diameter. The measured BET specific surface area, Langmuir specific surface area, and total pore volume of the synthesized sample (see Table 1) are close to those reported by Tagliabue et al. (2011). In order to reduce the pressure drop across the fixed-bed adsorber in the breakthrough experiments, the synthesized sample was pressed at 2 MPa and then crushed into particles with sizes from 0.420 to 0.595 mm in diameter. As shown in Table 1, the BET specific surface area, Langmuir specific surface area, and total pore volume of the pellet sample are only slightly reduced in comparison with those of the synthesized sample. This could be caused by a decrease in inter-crystallite or particle voids after pressed at 2 MPa (Alcaniz-Monge et al., 2009). Table 1 also includes the He grain density of the pellet sample, which will be used in simulations for the transient breakthroughs.

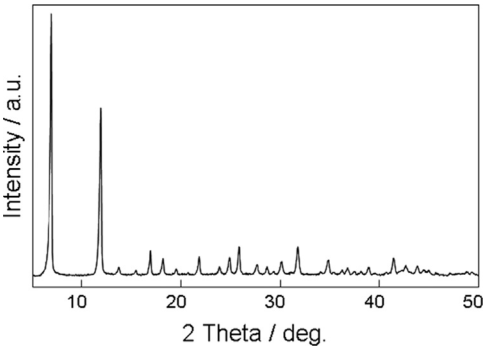

Fig. 3. XRD pattern of the synthesized Ni-MOF-74.

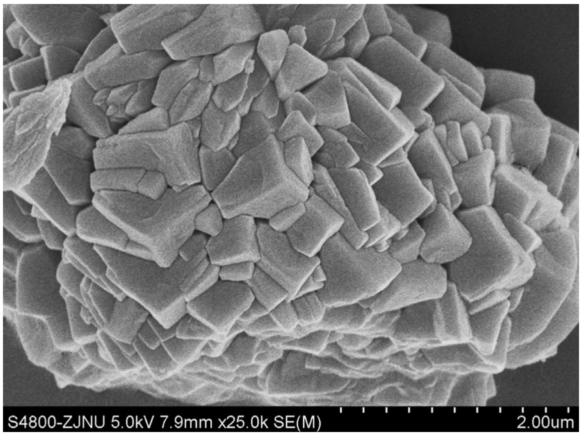

Fig. 4. SEM image of the synthesized Ni-MOF-74.

Table 1
Textural and physical properties of the synthesized Ni-MOF-74 and pellet samples.

Sample	S_{BET} ($m^2\,g^{-1}$)	$S_{Langmuir}$ ($m^2\,g^{-1}$)	V_{total} ($cm^3\,g^{-1}$)	He grain density ($kg\,m^{-3}$)
Synthesized	820	1083	0.41	
Pellet	733	967	0.36	2160

3.2. Adsorption isotherms

The adsorption isotherms of CO_2, CH_4, C_3H_6, and C_3H_8 on the pellet sample were measured at 298, 323, and 348 K, shown in Fig. 5. All the isotherms exhibit a type-I adsorption isotherm (Brunauer classification) over the temperature and pressure ranges studied. From a fundamental point of view, the experimental data should be correlated with an analytical expression that includes the temperature dependency. Various empirical methods have been proposed to fit isotherm data in adsorption science. In many cases, however, it may not be easy to determine a set of isotherm parameters that can represent all the experimental data at multiple temperatures with good accuracy. Therefore, we have used different isotherm models to fit the measured isotherm data and found that the Langmuir–Freundlich model describes the present case the best over the full range:

$$q = q_{sat}\frac{bp^{\nu}}{1+bp^{\nu}} \tag{1}$$

with T-dependent parameter b:

$$b = b_0 \exp\left(\frac{E}{RT}\right) \tag{2}$$

where q, q_{sat}, p, b, and ν represent the adsorbed amount, adsorption saturation capacity, pressure, equilibrium constant, and dimensionless parameter, respectively. b_0 is the value of b at infinite temperature and E is the energy change associated with adsorption. To avoid variant adsorption saturation capacity from the fitting at different temperatures, we fit the parameters (see Table 2) using the three sets of isotherms at the three different temperatures simultaneously. The fitted isotherms are shown in Fig. 5 as lines, in good agreement with experimental data.

In order to elucidate the differences in the adsorption of CO_2 and CH_4 on Ni-MOF-74, we take their isotherms at 298 K for

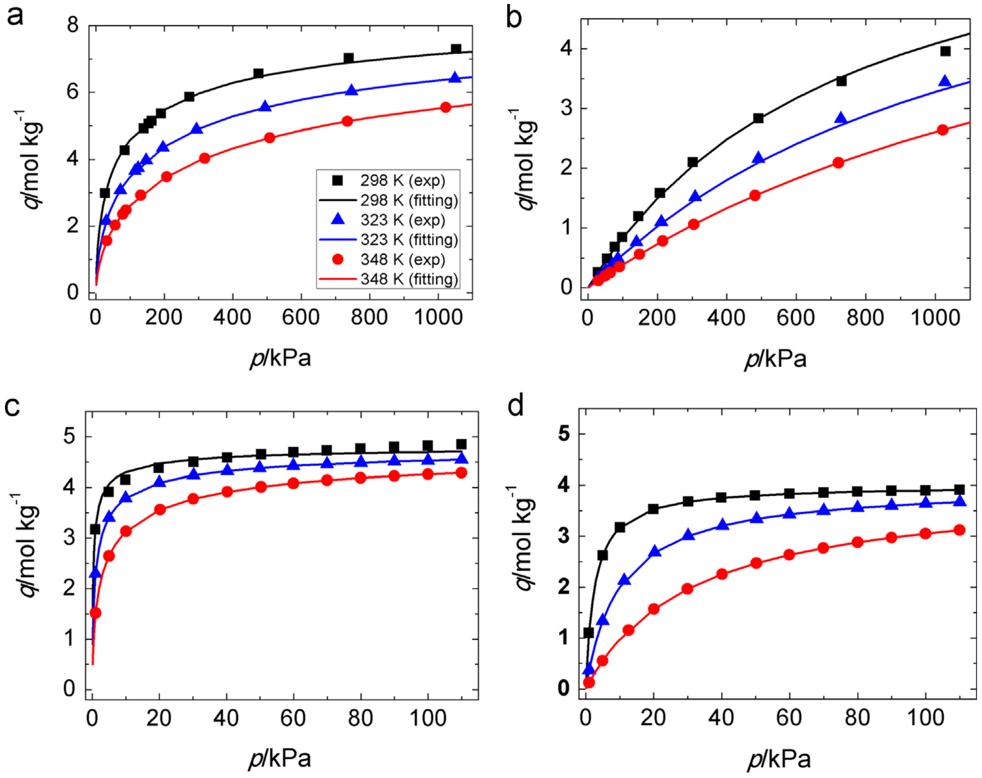

Fig. 5. Adsorption isotherms of CO_2 (a), CH_4 (b), C_3H_6 (c), and C_3H_8 (d) on the Ni-MOF-74 pellet adsorbent at 298 K (square), 323 K (triangle), and 348 K (circle), respectively. The lines are the Langmuir–Freundlich model correlations.

Table 2
Estimated parameter values for the combined fitting of the adsorption isotherm data of CO_2, CH_4, C_3H_6, and C_3H_8 on Ni-MOF-74 by the Langmuir–Freundlich model

Adsorbate	q_{sat} (mol kg^{-1})	b_0 (Pa$^{-\nu}$)	E (kJ mol^{-1})	ν
CO_2	8.8	1.51×10^{-6}	16.3	0.6
CH_4	7.2	3.78×10^{-9}	14.5	1.0
C_3H_6	4.85	1.15×10^{-6}	25.3	0.6
C_3H_8	4.0	3.11×10^{-11}	42.5	1.0

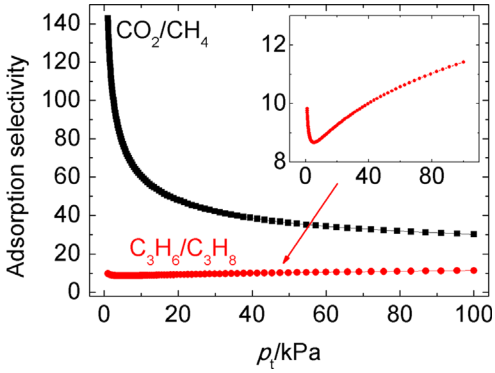

Fig. 6. IAST simulation for the adsorption selectivities for CO_2 over CH_4 and C_3H_6 over C_3H_8 of (50:50) CO_2/CH_4 and C_3H_6/C_3H_8 mixtures on Ni-MOF-74 at 298 K as a function of total pressure.

example, as shown in Fig. 5, the adsorbed amount of CH_4 increases almost linearly as a function of pressure, reaching 4.0 mol/kg at 1 MPa, much smaller than a predicted experimental saturation capacity of 7.2 mol/kg. In contrast to CH_4, the adsorbed amount of CO_2 increases sharply at pressures less than 100 kPa, at 100 kPa the adsorbed amount of CO_2 is 4.6 mol/kg, and then it gradually increases to 7.3 mol/kg with pressures up to 1 MPa, which is close to a predicted experimental saturation capacity of 8.8 mol/kg. The much higher adsorption affinity to CO_2 over CH_4 indicates that Ni-MOF-74 could be potentially used for the separation of CO_2/CH_4 mixtures, confirmed by the IAST calculations at 298 K showing CO_2/CH_4 adsorption selectivities in excess of 30 in the range of total pressures up to 100 kPa (Fig. 6).

The fitted isotherms of C_3H_6 and C_3H_8 agree very well with the experimental data (see Fig. 5). The experimental adsorption saturation capacities of C_3H_6 and C_3H_8 are predicted to be 4.85 and 4.0 mol/kg, respectively. By careful comparison of the isotherms between C_3H_6 and C_3H_8, we observe that the adsorbed amount of C_3H_6 is higher than that of C_3H_8 under the same conditions, especially in the low pressure range. This is due to the side-on π-coordination of C_3H_6 with the Ni^{2+}, whereas C_3H_8 is adsorbed to the metal site with much weaker interaction (Geier et al., 2013). Therefore, a high adsorption selectivity for C_3H_6 over C_3H_8 is expected in their binary mixture adsorption on Ni-MOF-74. Indeed, the IAST calculations at 298 K indicate that the selectivity for C_3H_6 over C_3H_8 is about 10 (Fig. 6).

3.3. Transient breakthrough experiments and comparisons with simulations

The breakthrough experiments were performed at three different temperatures (298, 323, and 348 K) and the exit pressure of the breakthrough column was set at 200 kPa. Fig. 7 shows the breakthrough profiles of C_3H_6 and C_3H_8 in He (C_3H_6: C_3H_8: He = 1:1:2 in mole ratio) through the fixed bed packed with the Ni-MOF-74 pellets, and the red and black symbols represent the mole fractions of C_3H_6 and C_3H_8 eluting through the column, respectively, as a function of time (t). For example, at 298 K, neither C_3H_6 nor C_3H_8 is detected at the outlet of the column when t is less than 800 s. As shown in Fig. 7, C_3H_8 elutes through

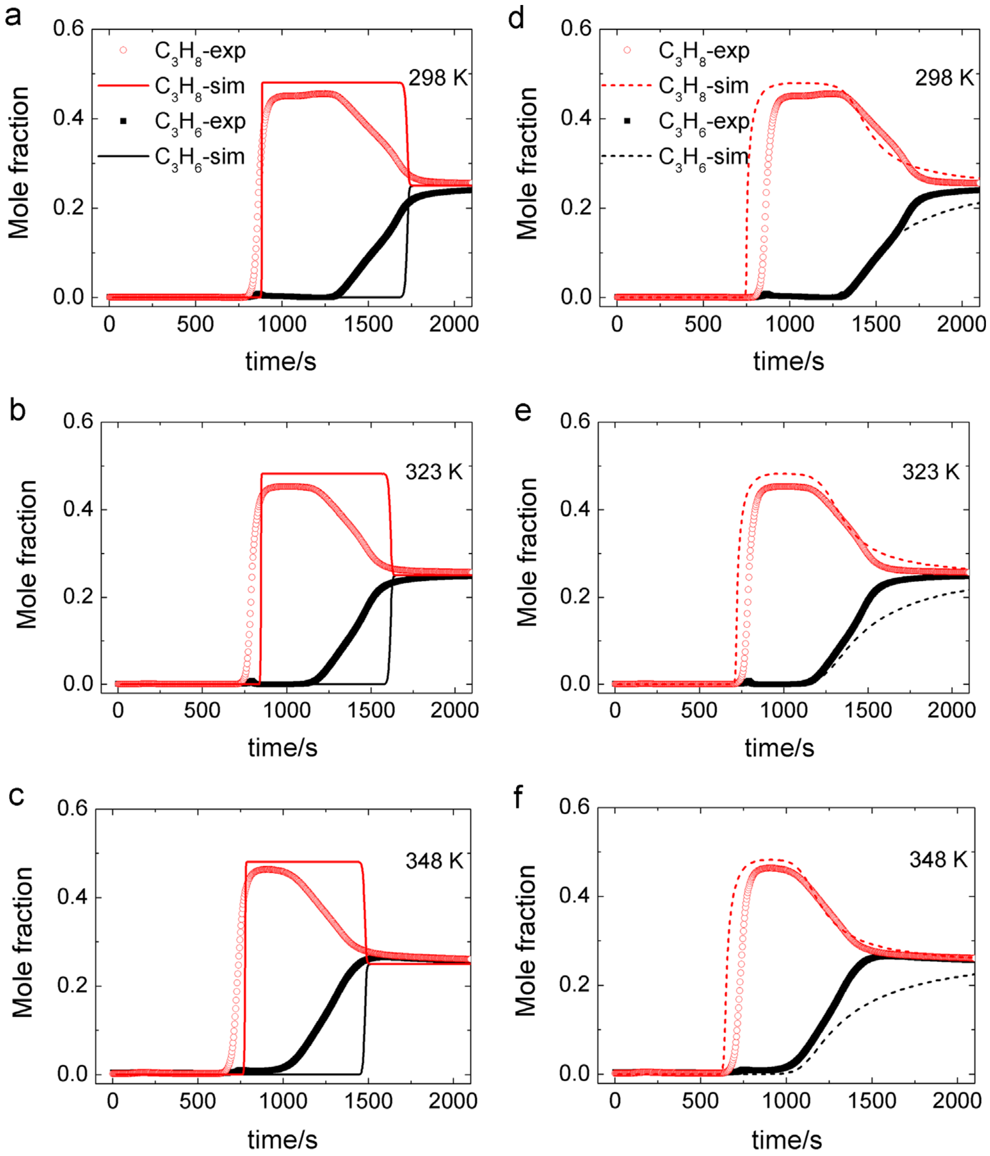

Fig. 7. Comparison of the experimental and simulated breakthrough curves for 1:1:2 C_3H_6/C_3H_8/He mixture at 298, 323, and 348 K, respectively. The simulated breakthrough curves without and with the consideration of intra-crystalline diffusion are shown at left (a–c) and right column (d–f), respectively, for comparison. The chosen diffusivity values are $Đ_1/r_c^2 = 2\times10^{-4}\ \mathrm{s}^{-1}$; $Đ_1/Đ_2 = 0.1$, where 1 and 2 represent C_3H_6 and C_3H_8, respectively. A video animation of the transient breakthrough at 298 K is available as the Supplementary material.

the column after 800 s and the mole fraction sharply increases to 0.45, higher than a mole fraction of 0.33 by assuming that the gas phase only consists of C_3H_8 and He and their flow rates are the same as those in the inlet of the column. This interesting phenomenon is ascribed to a competitive adsorption behavior between C_3H_6 and C_3H_8, resulting in the replacement of the adsorbed C_3H_8 by C_3H_6 due to the stronger adsorption affinity of C_3H_6.

Supplementary material related to this article can be found online at http://dx.doi.org/10.1016/j.ces.2014.07.008.

Transient breakthrough simulations were then performed to model the whole process with the same conditions as those in the experiments; the details of the breakthrough simulation methodology are provided as the Supplementary material accompanying this publication. The intra-crystalline diffusion was taken into account during the breakthrough simulations and compared to those without the consideration of diffusion to evaluate its effect. It is found that the assumption of the thermodynamic equilibrium at any position in the fixed-bed adsorber (i.e., the intra-crystalline diffusion is excluded) results in sharp breakthroughs for both C_3H_6 and C_3H_8, see Fig. 7(a–c), distinctly different from the experimentally determined breakthroughs with distended characteristics that are typical of intra-crystalline diffusion effects. For a quantitative comparison with the breakthrough experiments we then carried out simulations that include intra-crystalline diffusion effects, as explained in the Supplementary material. The chosen diffusivity values are $Đ_1/r_c^2 = 2\times10^{-4}\ \mathrm{s}^{-1}$; $Đ_2/r_c^2 = 2\times10^{-3}\ \mathrm{s}^{-1}$, where $Đ_1$,$Đ_2$, and r_c represent the Maxwell–Stefan diffusivities of C_3H_6 and C_3H_8 and the radius of the crystallites, respectively. The assumed diffusivity of C_3H_6 is taken to be a factor of 10 lower than that of the saturated alkane, because the stronger binding of C_3H_6 in Ni-MOF-74 leads to significantly lower diffusivities (Krishna and van Baten, 2012b, 2013). As seen in Fig. 7 (d–f), the inclusion of intra-crystalline into the simulations leads to distended breakthroughs, which are in better agreement with experiments. This indicates the inclusion of intra-crystalline diffusion is important for accurate description of the thermodynamic kinetics of

C_3H_6/C_3H_8 mixture. The above conclusions are also applicable to the other two temperatures 323 and 348 K. In all three cases, the consideration of intra-crystalline diffusion plays a key role in accurately describing the thermodynamic kinetics of C_3H_6/C_3H_8 mixture in Ni-MOF-74. We also notice that the time for equilibrium is decreased as the temperature changes from 298 to 323 and 348 K, which is reasonable since the adsorption capacity of the adsorbent is lower as the temperature increases. For each case, there is a certain period that pure C_3H_6 elutes through the bed, suggesting that Ni-MOF-74 adsorbent has very high separation efficiency for C_3H_6/C_3H_8 mixture in this regard.

In addition to its high separation selectivity for C_3H_6/C_3H_8 mixture, Ni-MOF-74 may also be promising in separating CO_2/CH_4 mixture based on their large difference of uptakes as discussed in the last section. As shown in Fig. 8, at all three different temperatures, CH_4 is the first to elute through the bed in a short time, whereas the solid adsorbent retains the CO_2. Take the breakthroughs at 298 K for example in order to explain the differences in breakthrough between CO_2 and CH_4, CH_4 at the outlet of column sharply increases to a mole fraction of 0.33 at time = 300 s, while no CO_2 gas is detected until the time is larger than 1300 s. This could be explained as the fact that the CO_2 molecules have much stronger adsorption strength in Ni-MOF-74 than CH_4 and thus they gradually occupy all possible adsorption sites. Interestingly, the ratio of CH_4 is larger than 0.25 (molar fraction at the inlet of column) in a large range of time from about 200 s to the end of the experiments. Two reasons may cause this roll-up effect: Firstly, the CO_2 molecules are completely adsorbed on the adsorbent and thus not detected at the outlet of the column at all, and therefore the ratio of CH_4 could reach a value of 0.33 (1:2 CH_4/He mixture). Secondly, the CO_2 molecules may have a competing adsorption behavior over CH_4 when the available adsorption sites in Ni-MOF-74 decrease, thus leading to an increase in the amount of CH_4 at the outlet of column.

Supplementary material related to this article can be found online at http://dx.doi.org/10.1016/j.ces.2014.07.008.

For a quantitative comparison with the breakthrough experiments we also carried out simulations without and with the inclusion of intra-crystalline diffusion effects, see Fig. 8 (a–c) and (d–f), respectively. The chosen diffusivity values are $\text{Đ}_1/r_c^2 = 1\times10^{-3}\ \mathrm{s}^{-1}$; $\text{Đ}_2/r_c^2 = 2\times10^{-2}\ \mathrm{s}^{-1}$ for CO_2 and CH_4, respectively. The diffusivity of

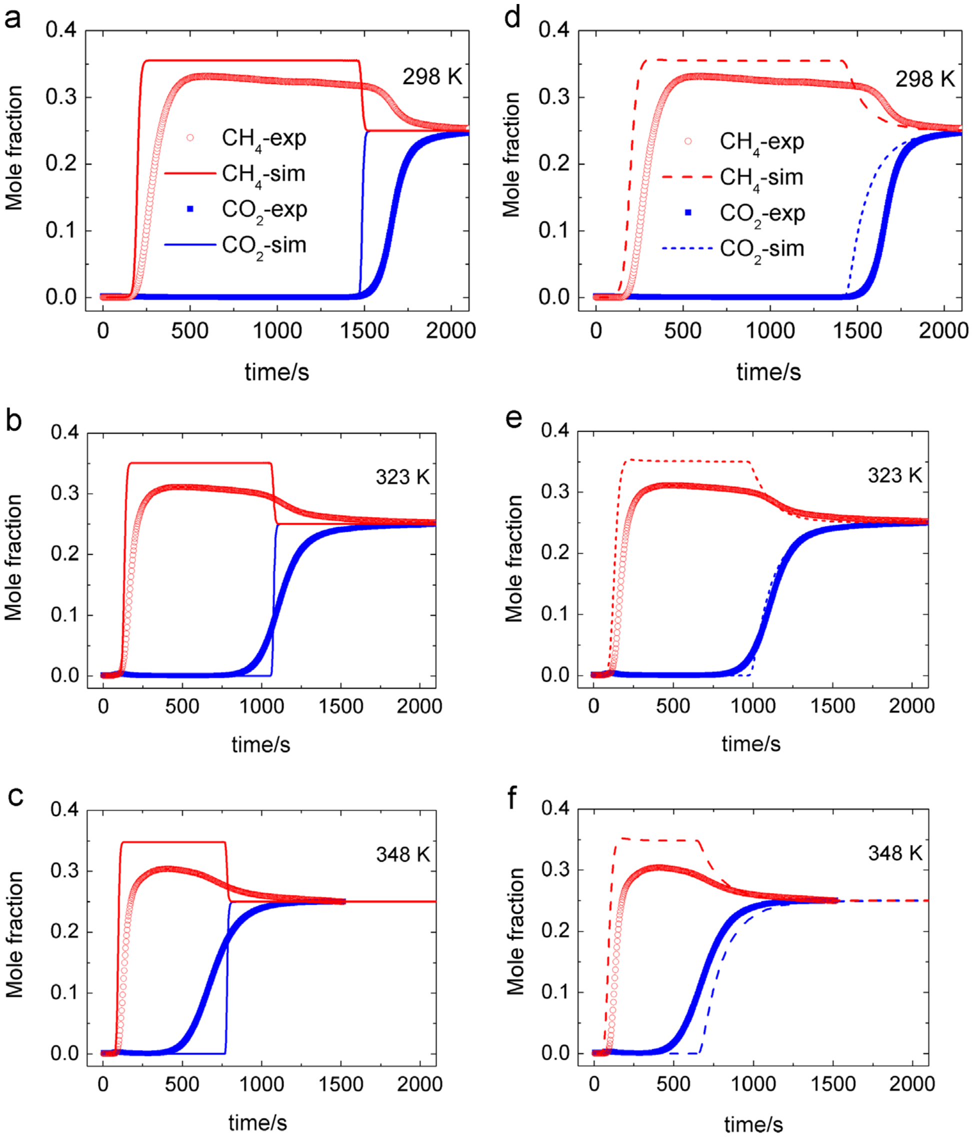

Fig. 8. Comparison of the experimental and simulated breakthrough curves for 1:1:2 CO_2/CH_4/He mixture at 298, 323, and 348 K, respectively. The simulated breakthrough curves without and with the consideration of intra-particle diffusion are shown at left (a–c) and right column (d–f), respectively, for comparison. The chosen diffusivity values are $\text{Đ}_1/r_c^2 = 1\times10^{-3}\ \mathrm{s}^{-1}$; $\text{Đ}_1/\text{Đ}_2 = 0.05$, where 1 and 2 represent CO_2 and CH_4, respectively. A video animation of the transient breakthrough at 298 K is available as the Supplementary Material.

CO_2 is chosen to be a factor 20 lower than that of CH_4 in order to reflect the strong influence of the binding energy on diffusivities (Krishna and van Baten, 2012b, 2013). Several useful conclusions are obtained: (1) the inclusion of intra-crystalline diffusion improves the quality of the simulated breakthrough curves, which are in better agreement with experiments; (2) the predicted mole fraction for CH_4 after its breakthrough transition reaches to a steady value of about 0.35, which is larger than the experimental values; the value of 0.35 is also larger than 0.33 (equilibrium state for 1:2 CH_4/He), which may arise from the competitive adsorption of CO_2 over CH_4. Note that a similar value of about 0.47 for C_3H_6/C_3H_8 is much larger than 0.35, which could be explained as the fact that the adsorbed amount of CH_4 is much smaller than CO_2, while the adsorbed C_3H_8 is not significantly smaller than C_3H_6 under the given condition, thus when competitive adsorption happens the increased mole fraction of CH_4 is not as large as that for C_3H_8. The simulated breakthrough and breakthrough experiments for the CO_2/CH_4 mixture confirm that the Ni-MOF-74 material is a potential candidate for separating gas mixtures.

Although breakthrough experiments are quite valuable for evaluating the gas separation capabilities of a material, in practice they can be difficult and time consuming. Assuming that (i) external mass transfer resistances and heat effects are negligible through an isothermal adsorption bed in thermodynamic equilibrium, (ii) plug flow proceeds through the bed, and (iii) the binary mixture adsorption equilibrium in the packed bed of adsorbent can be calculated using IAST, we were able to solve a set of partial differential equations and calculate breakthrough curves. Here we have demonstrated that the breakthrough characteristics could instead be simulated with reasonable accuracy. Given this validation, we can minimize breakthrough experimental work and employ analogous simulations to make quantitative comparisons with other materials. However, for a large- and/or industrial-scale PSA process, the modeling or simulation should include external and/or internal mass transfer resistances, axial dispersion, and heat effects. Recently, Ferreira et al. (in press) indeed developed a full model to simulate the measured single and binary breakthrough curves of a CO_2/CH_4 mixture on MIL-53 (Al).

4. Conclusions

The present study shows the potential application of Ni-MOF-74 with high density of the coordinatively unsaturated metal sites on selective separation of gas mixtures such as C_3H_6/C_3H_8 and CO_2/CH_4. To evaluate its practical applications we focus on studying the separation efficiency via breakthrough experiments as well as breakthrough simulations proposed recently, which have been proven to be a realistic tool for screening adsorbents for separations. The breakthrough results show that Ni-MOF-74 exhibits a high selectivity for CO_2 over CH_4 and for C_3H_6 over C_3H_8, thus producing pure CO_2 and C_3H_6 from CO_2/CH_4 and C_3H_6/C_3H_8 mixtures, respectively, under certain conditions. The simulations agree well with experiments when the intra-crystalline diffusion is taken into account, for all the mixtures investigated in this study.

Nomenclature

b	adsorption equilibrium constant in the Langmuir–Freundlich model, $Pa^{-\nu_i}$
b_0	adsorption equilibrium constant at infinite temperature, $Pa^{-\nu_i}$
E	adsorption energy change in the Langmuir–Freundlich model, $kJ\ mol^{-1}$
$Đ_i$	Maxwell–Stefan diffusivity, $m^2\ s^{-1}$
p	pressure, Pa
p_t	total pressure, Pa
q	adsorbed amount, $mol\ kg^{-1}$
q_{sat}	adsorption saturation capacity, $mol\ kg^{-1}$
R	universal gas constant, $8.314\ J\ mol^{-1}\ K^{-1}$
r_c	radius of crystallite, m
S_{BET}	BET specific surface area, $m^2\ g^{-1}$
$S_{Langmuir}$	Langmuir specific surface area, $m^2\ g^{-1}$
t	time, s
T	absolute temperature, K
V_{total}	total pore volume of sample, $cm^3\ g^{-1}$

Greek letters

ν	exponent in the Langmuir–Freundlich model, dimensionless

Acknowledgment

W.Z. and D.C. gratefully acknowledge the financial support from the National Natural Science Foundation of China (21036006 and 21303165).

Appendix A. Supplementary material

Supplementary data associated with this article can be found in the online version at http://dx.doi.org/10.1016/j.ces.2014.07.008.

References

Alcaniz-Monge, J., Trautwein, G., Perez-Cadenas, M., Roman-Martinez, M.C., 2009. Effects of compression on the textural properties of porous solids. Microporous Mesoporous Mater. 126, 291–301.

Alivisatos, P., Buchanan, M., 2010. Basic Research Needs for Carbon Capture: Beyond 2020U.S. Department of Energy, Office of Science, Basic Energy Sciences.

Banerjee, R., Phan, A., Wang, B., Knobler, C., Furukawa, H., O'Keeffe, M., Yaghi, O.M., 2008. High-throughput synthesis of zeolitic imidazolate frameworks and application to CO_2 capture. Science 319, 939–943.

Bao, Z., Alnemrat, S., Vasiliev, I., Ren, Q., Yu, L., Lu, X., Deng, S., 2011a. Adsorption of ethane, ethylene, propane and propylene on a magnesium-based metal-organic framework. Langmuir 27, 13554–13562.

Bao, Z., Yu, L., Ren, Q., Lu, X., Deng, S., 2011b. Adsorption of CO_2 and CH_4 on a magnesium-based metal organic framework. J. Colloid Interface Sci. 353, 549–556.

Bloch, E.D., Queen, W.L., Krishna, R., Zadrozny, J.M., Brown, C.M., Long, J.R., 2012. Hydrocarbon separations in a metal-organic framework with open iron(II) coordination sites. Science 335, 1606–1610.

Böhme, U., Barth, B., Paula, C., Kuhnt, A., Schwieger, W., Alexander Mundstock, A., Caro, J., Hartmann, M., 2013. Ethene/ethane and propene/propane separation via the olefin and paraffin selective metal-organic framework adsorbents CPO-27 and ZIF-8. Langmuir 29, 8592–8600.

Britt, D., Tranchemontagne, D., Yaghi, O.M., 2008. Metal-organic frameworks with high capacity and selectivity for harmful gases. Proc. Natl. Acad. Sci. USA 105, 11623–11627.

Bux, H., Chmelik, C., Krishna, R., Caro, J., 2011. Ethene/ethane separation by the MOF membrane ZIF-8: molecular correlation of permeation, adsorption, diffusion. J. Membr. Sci. 369, 284–289.

Caskey, S.R., Wong-Foy, A.G., Matzger, A.J., 2008. Dramatic tuning of carbon dioxide uptake via metal substitution in a coordination polymer with cylindrical pores. J. Am. Chem. Soc. 130, 10870–10871.

Chavan, S., Bonino, F., Valenzano, L., Civalleri, B., Lamberti, C., Acerbi, N., Cavka, J.H., Leistner, M., Bordiga, S., 2013. Fundamental aspects of H_2S adsorption on CPO-27-Ni. J. Phys. Chem. C 117, 15615–15622.

Chmelik, C., van Baten, J.M., Krishna, R., 2012. Hindering effects in diffusion of CO_2/CH_4 mixtures in ZIF-8 crystals. J. Membr. Sci. 397–398, 87–91.

Da Silva, F.A., Rodrigues, A.E., 1999. Adsorption equilibria and kinetics for propylene and propane over 13X and 4A zeolite pellets. Ind. Eng. Chem. Res. 38, 2051–2057.

Dietzel, P.D.C., Johnsen, R.E., Fjellvåg, H., Bordiga, S., Groppo, E., Chavan, S., Blom, R., 2008. Adsorption properties and structure of CO_2 adsorbed on open coordination sites of metal-organic framework Ni_2(dhtp) from gas adsorption, IR spectroscopy and X-ray diffraction. Chem. Commun., 5125–5127.

Dietzel, P.D.C., Panella, B., Hirscher, M., Blom, R., Fjellvåg, H., 2006. Hydrogen adsorption in a nickel based coordination polymer with open metal sites in the cylindrical cavities of the desolvated framework. Chem. Commun., 959–961.

Duan, J., Higuchi, M., Krishna, R., Kiyonaga, T., Tsutsumi, Y., Sato, Y., Kubota, Y., Takata, M., Kitagawa, S., 2014. High $CO_2/N_2/O_2/CO$ separation in a chemically robust porous coordination polymer with low binding energy. Chem. Sci. 5, 660–666.

Eldridge, R.B., 1993. Olefin/paraffin separation technology: a review. Ind. Eng. Chem. Res. 32, 2208–2212.

Ferey, G., 2008. Hybrid porous solids: past, present, future. Chem. Soc. Rev. 37, 191–214.

Ferreira A.F.P., Mafalda Ribeiro A., Kulaç S. Rodrigues A.E., Methane purification by adsorptive processes on MIL-53(Al), Chem. Eng. Sci. http://dx.doi.org/10.1016/j.ces.2014.06.014, in press.

Furukawa, H., Cordova, K.E., O'Keeffe, M., Yaghi, O.M., 2013. The chemistry and applications of metal-organic frameworks. Science 341, 2040–2042.

Geier, S.J., Mason, J.A., Bloch, E.D., Queen, W.L., Hudson, M.R., Brown, C.M., Long, J.R., 2013. Selective adsorption of ethylene over ethane and propylene over propane in the metal-organic frameworks M_2(dobdc) (M = Mg, Mn, Fe, Co, Ni, Zn). Chem. Sci. 4, 2054–2061.

Gucuyener, C., van den Bergh, J., Gascon, J., Kapteijn, F., 2010. Ethane/ethene separation turned on its head: selective ethane adsorption on the metal-organic framework ZIF-7 through a gate-opening mechanism. J. Am. Chem. Soc. 132, 17704–17706.

Haldoupis, E., Nair, S., Sholl, D.S., 2010. Efficient calculation of diffusion limitations in metal organic framework materials: a tool for identifying materials for kinetic separations. J. Am. Chem. Soc. 132, 7528–7539.

He, Y., Krishna, R., Chen, B., 2012. Metal-organic frameworks with potential for energy-efficient adsorptive separation of light hydrocarbons. Energy Environ. Sci. 5, 9107–9120.

Herm, Z.R., Krishna, R., Long, J.R., 2012. CO_2/CH_4, CH_4/H_2 and $CO_2/CH_4/H_2$ separations at high pressures using Mg_2(dobdc). Microporous Mesoporous Mater. 151, 481–487.

Herm, Z.R., Swisher, J.A., Smit, B., Krishna, R., Long, J.R., 2011. Metal-organic frameworks as adsorbents for hydrogen purification and pre-combustion carbon dioxide capture. J. Am. Chem. Soc. 133, 5664–5667.

Kim, H., Jung, Y., 2014. Can metal-organic framework separate 1-butene from butene isomers? J. Phys. Chem. Lett. 5, 440–446.

Kim, H., Park, J., Jung, Y., 2013. The binding nature of light hydrocarbons on Fe/MOF-74 for gas separation. Phys. Chem. Chem. Phys. 15, 19644–19650.

Kizzie, A.C., Wong-Foy, A.G., Matzger, A.J., 2011. Effect of humidity on the performance of microporous coordination polymers as adsorbents for CO_2 Capture. Langmuir 27, 6368–6373.

Krishna, R., 2014. The Maxwell–Stefan description of mixture diffusion in nanoporous crystalline materials. Microporous Mesoporous Mater. 185, 30–50.

Krishna, R., van Baten, J.M., 2010. In silico screening of zeolite membranes for CO_2 capture. J. Membr. Sci. 360, 323–333.

Krishna, R., van Baten, J.M., 2011a. In silico screening of metal-organic frameworks in separation applications. Phys. Chem. Chem. Phys. 13, 10593–10616.

Krishna, R., van Baten, J.M., 2011b. A molecular dynamics investigation of the diffusion characteristics of cavity-type zeolites with 8-ring windows. Microporous Mesoporous Mater. 137, 83–91.

Krishna, R., van Baten, J.M., 2012a. A comparison of the CO_2 capture characteristics of zeolites and metal-organic frameworks. Sep. Purif. Method 87, 120–126.

Krishna, R., van Baten, J.M., 2012b. Investigating the relative influences of molecular dimensions and binding energies on diffusivities of guest species inside nanoporous crystalline materials. J. Phys. Chem. C 116, 23556–23568.

Krishna, R., van Baten, J.M., 2013. Influence of adsorption thermodynamics on guest diffusivities in nanoporous crystalline materials. Phys. Chem. Chem. Phys. 15, 7994–8016.

Li, J.-R., Sculley, J., Zhou, H.-C., 2012. Metal-organic framework for separations. Chem. Rev. 112, 869–932.

Li, K.H., Olson, D.H., Seidel, J., Emge, T.J., Gong, H.W., Zeng, H.P., Li, J., 2009. Zeolitic imidazolate frameworks for kinetic separation of propane and propene. J. Am. Chem. Soc. 131, 10368–10369.

Liu, J., Thallapally, P.K., McGrail, B.P., Brown, D.R., Liu, J., 2012. Progress in adsorption-based CO_2 capture by metal-organic frameworks. Chem. Soc. Rev. 41, 2308–2322.

Liu, J., Wang, Y., Benin, A.I., Jakubczak, P., Willis, R.R., LeVan, M.D., 2010. CO_2/H_2O adsorption equilibrium and rates on metal-organic frameworks: HKUST-1 and Ni/DOBDC. Langmuir 26, 14301–14307.

Mason, J.A., Sumida, K., Herm, Z.R., Krishna, R., Long, J.R., 2011. Evaluating metal-organic frameworks for post-combustion carbon dioxide capture via temperature swing adsorption. Energy Environ. Sci. 4, 3030–3040.

McDonald, T.M., D'Alessandro, D.M., Krishna, R., Long, J.R., 2011. Enhanced carbon dioxide capture upon incorporation of N,N-dimethylethylenediamine in the metal-organic framework CuBTTri. Chem. Sci. 2, 2022–2028.

Nijem, N., Wu, H.H., Canepa, P., Marti, A., Balkus, K.J., Thonhauser, T., Li, J., Chabal, Y.J., 2012. Tuning the gate opening pressure of metal-organic frameworks (MOFs) for the selective separation of hydrocarbons. J. Am. Chem. Soc. 134, 15201–15204.

Padurean, A., Cormos, C.C., Agachi, P.S., 2012. Pre-combustion carbon dioxide capture by gas–liquid absorption for integrated gasification combined cycle power plants. Int. J. Greenh. Gas Control 7, 1–11.

Palomino, M., Cantín, A., Corma, A., Leiva, S., Rey, F., Valencia, S., 2007. Pure silica ITQ-32 zeolite allows separation of linear olefins from paraffins. Chem. Commun., 1233–1235.

Sumida, K., Rogow, D.L., Mason, J.A., McDonald, T.M., Bloch, E.D., Herm, Z.R., Bae, T.-H., Long, J.R., 2012. Carbon dioxide capture in metal organic frameworks. Chem. Rev. 112, 724–781.

Tagliabue, M., Rizzo, C., Millini, R., Dietzel, P.D.C., Blom, R., Zanardi, S., 2011. Methane storage on CPO-27-Ni pellets. J. Porous Mater. 18, 289–296.

van Miltenburg, A., Gascon, J., Zhu, W., Kapteijn, F., Moulijn, J.A., 2008. Propylene/propane mixture adsorption on faujasite sorbents. Adsorption 14, 309–321.

Watanabe, T., Keskin, S., Nair, S., Sholl, D.S., 2009. Computational identification of a metal organic framework for high selectivity membrane-based CO_2/CH_4 separations: Cu(hfipbb)$(H_2hfipbb)_{0.5}$. Phys. Chem. Chem. Phys. 11, 11389–11394.

Wu, H., Simmons, J.M., Srinivas, G., Zhou, W., Yildirim, T., 2010. Adsorption sites and binding nature of CO_2 in prototypical metal-organic frameworks: a combined neutron diffraction and first-principles study. J. Phys. Chem. Lett. 1, 1946–1951.

Wu, H.H., Yao, K.X., Zhu, Y.H., Li, B.Y., Shi, Z., Krishna, R., Li, J., 2012. Cu-TDPAT, an rht-type dual-functional metal-organic framework offering significant potential for use in H_2 and natural gas purification processes operating at high pressures. J. Phys. Chem. C 116, 16609–16618.

Wu, X., Bao, Z., Yuan, B., Wang, J., Sun, Y., Luo, H., Deng, S., 2014. Microwave synthesis and characterization of MOF-74 (M = Ni, Mg) for gas separation. Microporous Mesoporous Mater. 180, 114–122.

Xiang, S.C., He, Y.B., Zhang, Z.J., Wu, H., Zhou, W., Krishna, R., Chen, B.L., 2012. Microporous metal-organic framework with potential for carbon dioxide capture at ambient conditions. Nat. Commun. 3, 954.

Yaghi, O.M., O'Keeffe, M., Ockwig, N.W., Chae, H.K., Eddaoudi, M., Kim, J., 2003. Reticular synthesis and the design of new materials. Nature 423, 705–714.

Yang, J.F., Krishna, R., Li, J.M., Li, J.P., 2014. Experiments and simulations on separating a CO_2/CH_4 mixture using K-KFI at low and high pressures. Microporous Mesoporous Mater. 184, 21–27.

Yu, D.C., Yazaydin, A.O., Lane, J.R., Dietzel, P.D.C., Snurr, R.Q., 2013. A combined experimental and quantum chemical study of CO_2 adsorption in the metal-organic framework CPO-27 with different metals. Chem. Sci. 4, 3544–3556.

Zhu, W., Kapteijn, F., Moulijn, J.A., 1999. Shape selectivity in the adsorption of propane/propene on the all-silica DD3R. Chem. Commun., 2453–2454.

Zhu, W., Kapteijn, F., Moulijn, J.A., den Exter, M.C., Jansen, J.C., 2000. Shape selectivity in adsorption on the all-silica DD3R. Langmuir 16, 3322–3329.

Supplementary Material to accompany

Transient Breakthroughs of CO_2/CH_4 and C_3H_6/C_3H_8 Mixtures in Fixed Beds Packed with Ni-MOF-74

De-Li Chen,[1] Hao Shang,[1] Weidong Zhu,[1*] and Rajamani Krishna[2*]

[1]Key Laboratory of the Ministry of Education for Advanced Catalysis Materials, Institute of Physical Chemistry, Zhejiang Normal University, 321004 Jinhua, P. R. of China.

[2]Van ‘t Hoff Institute for Molecular Sciences, University of Amsterdam, Science Park 904,

1098 XH Amsterdam, The Netherlands

1. Simulation methodology for transient breakthrough in fixed bed adsorbers

Fixed bed, packed with crystals of nanoporous materials, are commonly used for separation of mixtures (see schematic in Figure **1**); such adsorbers are commonly operated in a transient mode, and the compositions of the gas phase, and within the crystals, vary with position and time. Experimental data on the transient breakthrough of mixtures across fixed beds are commonly used to evaluate and compare the separation performance of zeolites and MOFs.[1-5] For a given separation task, transient breakthroughs provide more a realistic evaluation of the efficacy of a material, as they reflect the combined influence of adsorption selectivity, and adsorption capacity.[5, 6]

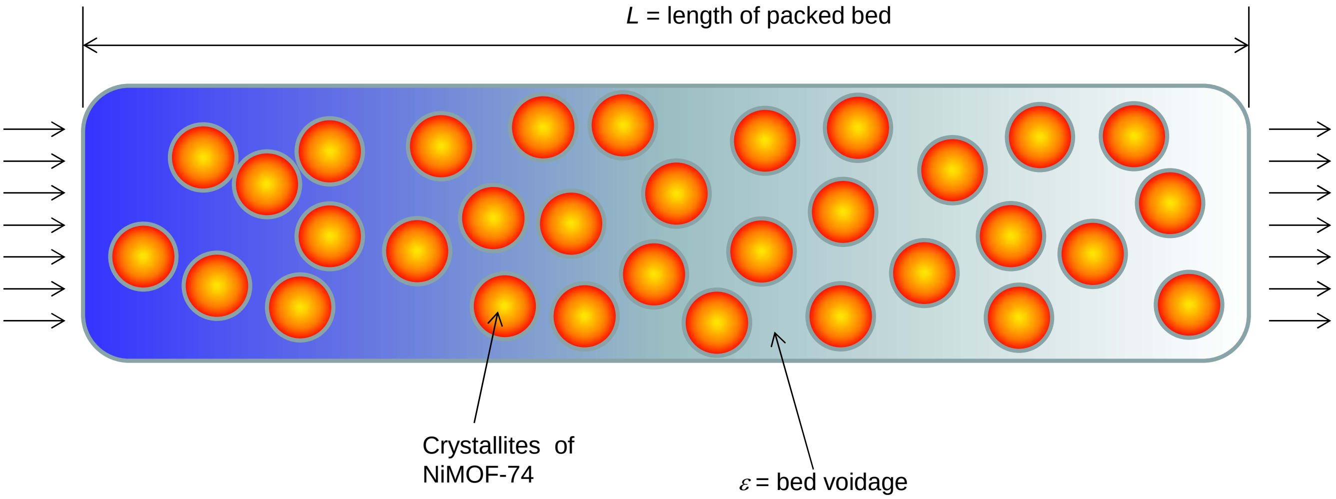

Figure 1. Schematic of a packed bed adsorber.

The transient breakthrough characteristics of CO_2/CH_4, and C_3H_6/C_3H_8 mixtures were measured in a breakthrough set-up with the following dimensions: inner diameter: 4.65 mm, length: 100 mm, CPO-

27-Ni loaded amount: 576.1 mg, particle sizes: 0.420-0.595 mm in diameter, particle density: 2160 kg m^{-3}.

Transient breakthroughs are influenced by both mixture adsorption equilibrium, and intra-crystalline diffusion. In order to determine the extent of the relative importance of adsorption and diffusion in determining the separation performance we perform transient breakthrough simulations, and compare these with experimental data. We describe below the simulation methodology used to perform transient breakthrough calculations.

Assuming plug flow of an *n*-component gas mixture through a fixed bed maintained under isothermal conditions, the partial pressures in the gas phase at any position and instant of time are obtained by solving the following set of partial differential equations for each of the species *i* in the gas mixture.[7]

$$\frac{1}{RT}\frac{\partial p_i(t,z)}{\partial t} = -\frac{1}{RT}\frac{\partial \left(v(t,z)p_i(t,z)\right)}{\partial z} - \frac{(1-\varepsilon)}{\varepsilon}\rho\frac{\partial \overline{q}_i(t,z)}{\partial t}; \quad i = 1,2,...n \tag{1}$$

In equation (1), t is the time, z is the distance along the adsorber, ρ is the framework density, ε is the bed voidage, v is the interstitial gas velocity, and $\overline{q}_i(t,z)$ is the *spatially averaged* molar loading within the crystallites of radius r_c, monitored at position z, and at time t.

At any time t, during the transient approach to thermodynamic equilibrium, the spatially averaged molar loading within the crystallite r_c is obtained by integration of the radial loading profile

$$\overline{q}_i(t) = \frac{3}{r_c^3}\int_0^{r_c} q_i(r,t)r^2 dr \tag{2}$$

For transient unary uptake within a crystal at any position and time with the fixed bed, the radial distribution of molar loadings, q_i, within a spherical crystallite, of radius r_c, is obtained from a solution of a set of differential equations describing the uptake

$$\frac{\partial q_i(r,t)}{\partial t} = -\frac{1}{\rho}\frac{1}{r^2}\frac{\partial}{\partial r}\left(r^2 N_i\right) \tag{3}$$

The molar flux N_i of component *i* is described by the simplified version of the Maxwell-Stefan equations in which both correlation effects and thermodynamic coupling effects are considered to be of negligible importance[5]

$$N_i = -\rho Đ_i \frac{\partial q_i}{\partial r} \tag{4}$$

Summing equation (**2**) over all *n* species in the mixture allows calculation of the *total average* molar loading of the mixture within the crystallite

$$\overline{q}_t(t,z) = \sum_{i=1}^{n} \overline{q}_i(t,z) \tag{5}$$

The *interstitial* gas velocity is related to the *superficial* gas velocity by

$$v = \frac{u}{\varepsilon} \tag{6}$$

In industrial practice, the most common operation is with to use a step-wise input of mixtures to be separation into an adsorber bed that is initially free of adsorbates, i.e. we have the initial condition

$$t = 0; \quad q_i(0,z) = 0 \tag{7}$$

At time, $t = 0$, the inlet to the adsorber, $z = 0$, is subjected to a step input of the *n*-component gas mixture and this step input is maintained till the end of the adsorption cycle when steady-state conditions are reached.

$$t \geq 0; \quad p_i(0,t) = p_{i0}; \quad u(0,t) = u_0 \tag{8}$$

where u_0 is the superficial gas velocity at the inlet to the adsorber.

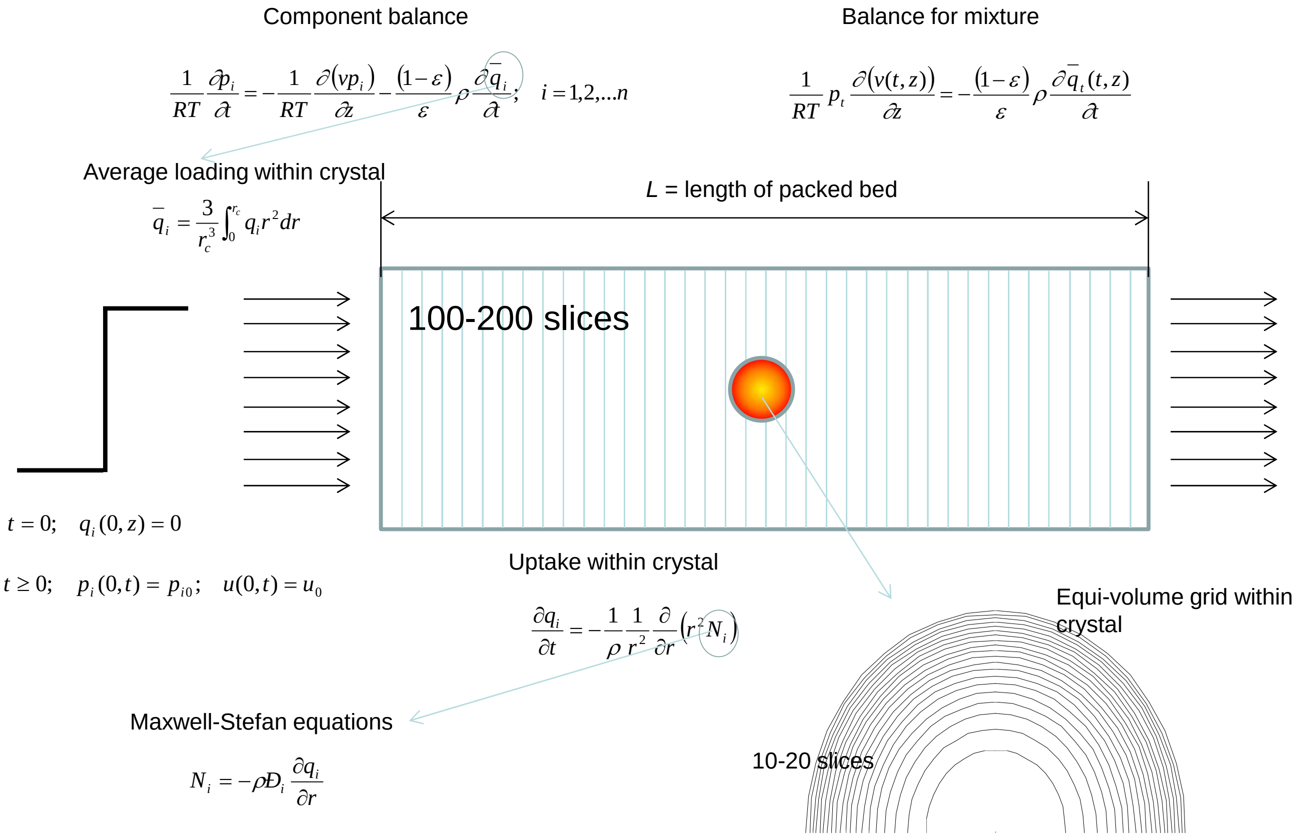

Figure 2. Summary of model equations describing packed bed adsorber, along with discretization scheme.

For convenience, the set of equations describing the fixed bed adsorber are summarized in Figure 2. Typically, the adsorber length is divided into 100 – 200 slices. Combination of the discretized partial differential equations (PDEs) along with the algebraic IAST or RAST equilibrium model, results in a set of differential-algebraic equations (DAEs), which are solved using BESIRK.[8] BESIRK is a sparse matrix solver, based on the semi-implicit Runge-Kutta method originally developed by Michelsen,[9] and extended with the Bulirsch-Stoer extrapolation method.[10] Use of BESIRK improves the numerical solution efficiency in solving the set of DAEs. The evaluation of the sparse Jacobian required in the numerical algorithm is largely based on analytic expressions.[7] Further details of the numerical procedures used in this work, are provided by Krishna and co-workers;[7, 11-13] interested readers are referred to our website that contains the numerical details.[11]

If the value of $\frac{Đ_i}{r_c^2}$ is large enough to ensure that intra-crystalline gradients are absent and the entire crystallite particle can be considered to be in thermodynamic equilibrium with the surrounding bulk gas phase at that time t, and position z of the adsorber

$$\overline{q}_i(t,z) = q_i(t,z) \tag{9}$$

The molar loadings at the *outer surface* of the crystallites, i.e. at $r = r_c$, are calculated on the basis of adsorption equilibrium with the bulk gas phase partial pressures p_i at that position z and time t. The adsorption equilibrium can be calculated on the basis of the IAST.

When matching experimental data on breakthroughs, the parameter values used correspond to those relevant to the experiments being simulated. Two types of breakthrough simulations were performed for each experimental run: (a) including diffusional limitations with assumed values of $\frac{Đ_i}{r_c^2}$ for matching with experimental breakthroughs, and (b) assuming negligible diffusional limitations and invoking equations (9).

In the breakthrough simulations reported in the main manuscript, we use (a) the same dimensions as in the experimental set-up, (b) the same sample mass, and (c) the same interstitial gas velocity as in the experiments.

2. Notation

c_i	molar concentration of species *i* in gas mixture, mol m^{-3}
c_{i0}	molar concentration of species *i* in gas mixture at inlet to adsorber, mol m^{-3}
c_t	total pore concentration in adsorbed mixture, mol m^{-3}
$Đ_i$	Maxwell-Stefan diffusivity, m^2 s^{-1}
L	length of packed bed adsorber, m
n	number of species in the mixture, dimensionless
N_i	molar flux of species *i*, mol m^{-2} s^{-1}
p_i	partial pressure of species *i* in mixture, Pa
p_t	total system pressure, Pa
q_i	component molar loading of species *i*, mol kg^{-1}
$q_{i,sat}$	molar loading of species *i* at saturation, mol kg^{-1}
q_t	total molar loading in mixture, mol kg^{-1}
q_{sat}	saturation loading, mol kg^{-1}
$\overline{q}_i(t)$	*spatially averaged* component molar loading of species *i*, mol kg^{-1}
r	radial direction coordinate, m
r_c	radius of crystallite, m
R	gas constant, 8.314 J mol^{-1} K^{-1}
t	time, s
T	absolute temperature, K
u	superficial gas velocity in packed bed, m s^{-1}
v	interstitial gas velocity in packed bed, m s^{-1}
z	distance along the adsorber, and along membrane layer, m

Greek letters

ε	voidage of packed bed, dimensionless

ρ	framework density, kg m^{-3}
τ	time, dimensionless

Subscripts

i	referring to component *i*
t	referring to total mixture

3. References

(1) Bloch, E. D.; Queen, W. L.; Krishna, R.; Zadrozny, J. M.; Brown, C. M.; Long, J. R. Hydrocarbon Separations in a Metal-Organic Framework with Open Iron(II) Coordination Sites, *Science* **2012**, *335*, 1606-1610.

(2) Herm, Z. R.; Wiers, B. M.; Van Baten, J. M.; Hudson, M. R.; Zajdel, P.; Brown, C. M.; Maschiocchi, N.; Krishna, R.; Long, J. R. Separation of Hexane Isomers in a Metal-Organic Framework with Triangular Channels *Science* **2013**, *340*, 960-964.

(3) Gücüyener, C.; van den Bergh, J.; Gascon, J.; Kapteijn, F. Ethane/Ethene Separation Turned on Its Head: Selective Ethane Adsorption on the Metal-Organic Framework ZIF-7 through a Gate-Opening Mechanism, *J. Am. Chem. Soc.* **2010**, *132*, 17704-17706.

(4) Yang, J.; Krishna, R.; Li, J.; Li, J. Experiments and Simulations on Separating a CO_2/CH_4 Mixture using K-KFI at Low and High Pressures, *Microporous Mesoporous Mater.* **2014**, *184*, 21-27.

(5) Krishna, R. The Maxwell-Stefan Description of Mixture Diffusion in Nanoporous Crystalline Materials, *Microporous Mesoporous Mater.* **2014**, *185*, 30-50.

(6) Krishna, R.; Long, J. R. Screening metal-organic frameworks by analysis of transient breakthrough of gas mixtures in a fixed bed adsorber, *J. Phys. Chem. C* **2011**, *115*, 12941-12950.

(7) Krishna, R.; Baur, R. Modelling issues in zeolite based separation processes, *Sep. Purif. Technol.* **2003**, *33*, 213-254.

(8) Kooijman, H. A.; Taylor, R. A dynamic nonequilibrium model of tray distillation columns, *A.I.Ch.E.J.* **1995**, *41*, 1852-1863.

(9) Michelsen, M. An efficient general purpose method of integration of stiff ordinary differential equations, *A.I.Ch.E.J.* **1976**, *22*, 594-597.

(10) Bulirsch, R.; Stoer, J. Numerical treatment of ordinary differential equations by extrapolation methods, *Numer. Math.* **1966**, *8*, 1-14.

(11) Krishna, R.; Baur, R. Diffusion, Adsorption and Reaction in Zeolites: Modelling and Numerical Issues, http://www.science.uva.nl/research/cr/zeolite/, University of Amsterdam, Amsterdam, 11 November 2003.

(12) Krishna, R.; van Baten, J. M. Investigating the potential of MgMOF-74 membranes for CO_2 capture, *J. Membr. Sci.* **2011**, *377*, 249-260.

(13) He, Y.; Krishna, R.; Chen, B. Metal-Organic Frameworks with Potential for Energy-Efficient Adsorptive Separation of Light Hydrocarbons, *Energy Environ. Sci.* **2012**, *5*, 9107-9120.